Ionospheric Chaos in Solar quiet Current due to Sudden Stratospheric Warming Events Across Europe-Africa Sector

Irewola Aaron, Oludehinwa[1,2,*]; Andrei, Velichko[3]; Olasunkanmi Isaac, Olusola[2]; Olawale

Segun, Bolaji[3,6]; Norbert, Marwan[4]; Babalola Olasupo, Ogunsua[5,7]; Abdullahi Ndzi, Njah[2];

Timothy Oluwaseyi Ologun[7].

1. Department of Physics, Caleb University, Lagos, Nigeria
2. Department of Physics, University of Lagos, Lagos, Nigeria
3. Institute of Physics and Technology, Petrozavodsk State University, 185910 Petrozavodsk, Russia.
4. Research Department of Complexity Science, Potsdam Institute for Climate Impact Research (PIK), Member of the Leibniz Association, 14412 Potsdam, Germany.
5. Key Laboratory for middle Atmospheric and Global Environment Observation (LAGEO), Institute of Atmospheric Physics (IAP), Chinese Academy of Science, Beijing, China.
6. Department of Physics, University of Tasmania, Australia.
7. Department of Physics, Federal University of Technology, Akure, Nigeria.
*Corresponding-Author:
    irewola.oludehinwa@calebuniversity.edu.ng; or Irewola2012@yahoo.com
    Tel.: +2348068030109

Abstract

This study examines the ionospheric chaos in the solar quiet current, $S_q(H)$ across Europe and

Africa sectors during 2009 and 2021 Sudden Stratospheric Warming (SSW) events. The SSW was

categorized into precondition, ascending, peak, descending, after and no-SSW phases based on the

rising stratospheric temperature. Thirteen magnetometer stations, located within the geographical

longitude of 26° to 40° across Europe and Africa sectors were considered. The magnetometer data

obtained during the periods of SSW were used to derived the solar quiet current time series. This

solar quiet current time series was transformed into a complex network using the HVG approach,

and Fuzzy Entropy was applied to the resulting node-degree time series to quantify the presence

of chaos or orderliness behavior in the ionosphere during SSW. The results revealed that the

latitudinal distribution of entropy in Europe sector depicts high entropy values indicating the

presence of ionospheric chaos. Consistent low entropy values unveiling the presence of orderliness

behavior were found to be prominent in the Africa sector. This dominance of orderliness behavior

during the phases of SSW in the Africa sector reveal that SSW effect manifest orderliness behavior

on the regional ionosphere of Africa sector. While, the pronounced features of ionospheric chaos

found in the European sector reveal evidence of significant effects of SSW on the regional

ionosphere in this sector. Finally, we found that after the peak phase of SSW, the ionospheric chaos

is more pronounced.

Keywords: Sudden Stratospheric Warming (SSW), Solar quiet current $S_q(H)$, Ionospheric

chaos, Fuzzy Entropy, Horizontal Visibility Graph (HVG

1. Introduction.

The chaotic behavior of the ionosphere dominates due to the complex interaction between the

lower and upper atmospheric circulation. This complex interaction is influenced by geographical

location, solar activity, and atmospheric dynamics. One of the lower atmospheric events capable

of causing global disruptions to the ionosphere is Sudden Stratospheric Warming (SSW). SSW is

one of the usual meteorological events, where the stratospheric temperature increases rapidly in

the winter polar region due to the rapid growth of quasi-stationary planetary waves from the

troposphere (Baldwin et al., 2021; Butler et al., 2015). The connections between the troposphere

and stratosphere during SSW introduces upward wave energy propagation that can reshape the

plasma density variability in the ionosphere. The dominant mechanism facilitating the connection

of these processes include planetary waves, atmospheric tides, and gravity waves (Goncharenko

et al., 2021; Chau et al., 2012; Goncharenko et al., 2010, 2012; Liu et al., 2010).

The SSW effect introduces spatial and temporal variability in the ionospheric plasma density (Yamazaki, 2013, 2014; Klimenko et al., 2018). As a result, the ionosphere exhibits nonlinear dynamical behavior, characterized by high sensitivity to minor perturbations originating from the lower atmosphere that could lead to transitions between orderliness and chaotic behavior of ionosphere, rendering its state susceptible to sudden and significant changes.

In the studies of dynamical systems such as logistic map, chaotic behavior is strongly associated with high entropy measures while orderliness behavior is associated with a declining and low entropy measures (Conejero et al., 2024). This observation forms the basis of this study, to quantitatively examine the dynamical behavior of the ionosphere during SSW across European and African sector. The regional ionosphere of European and Africa sectors manifest pronounced ionospheric variability in response to SSW events. For example, proximity to the geomagnetic equator in Africa could lead to different responses compared to higher latitude regions in Europe. This phenomenon provides a unique opportunity to investigate the complex coupling mechanisms between the stratosphere and ionosphere. Specifically, it enables the study of atmospheric wave propagation and its impact on the ionosphere, which can lead to disruptions in satellite communication and navigation system in the region.

One of the atmospheric parameters that can reveal the extent of the SSW-induced effects on the regional ionosphere is the solar quiet current, $S_q(H)$. During SSW event, planetary waves and tidal interactions can generate an electromotive force that drives the ionospheric current system (Yamazaki and Richmond, 2013; Yamazaki and Maute, 2017). These ionospheric currents during geomagnetically quiet periods are referred to as Solar quiet currents (S_q). They serve as a key phenomenon that manifest the degree of connection between the lower atmosphere and the ionosphere.

Several studies have already investigated the solar quiet current during SSW (Yamazaki, 2014; Bolaji et al., 2016a; Yamazaki and Maute, 2017; Yamazaki et al., 2011). For instance, Fejer et al. (2011) found enhanced lunar semi-diurnal vertical plasma drift amplitudes during early morning solar flux warming, associated with SSW. Maute et al. (2014) observed changes in ionospheric vertical drifts during SSW, attributing them to interactions between specific tides and planetary waves. Yamazaki et al. (2012a) studied the ionospheric current system during the 2002-2003 SSW events over East Asia, finding an additional current system superposed on the normal Sq current system. They attributed this to abnormally large lunar tidal winds, which also produced a counter electrojet (CEJ). Yamazaki et al. (2012b) examined the solar quiet current during SSW, finding significant hemispheric asymmetry: decreased intensity in the Northern Hemisphere and increased intensity in the Southern Hemisphere, accompanied by reduced longitudinal separation between the hemispheric eddies. Yamazaki, (2014) studied the solar and lunar ionospheric tidal forces, which are believed to influence ionospheric electrodynamics during SSW. By analyzing the average solar and lunar ionospheric current systems during SSW and non-SSW periods, he discovered that the intensity of lunar currents increases by roughly 75% during SSWs, whereas the solar current intensity is only slightly diminished, by approximately 10%. Bolaji et al. (2016b) investigated the solar quiet current response in Africa during SSW, categorizing temperature rises into six phases. A counter electrojet formed after peak SSW, and Sq(H) magnitude decreased between 21.13°N (Fayum, Egypt) and 39.51°S (Durban, South Africa) was observed. Siddiqui et al. (2018) examined the Equatorial Electrojet (EEJ) during major SSW events, finding a significant increase in the amplitude of EEJ semidiurnal lunar tides during SSW. Klimenko et al. (2019) investigated the impact of the 2009 SSW on the tropical lower thermosphere-ionosphere. They found that perturbations in ionospheric conductivity significantly contribute to the electric field

response to SSW. Additionally, the phase change of the semidiurnal solar tide (SW2) in neutral winds played a crucial role in shaping the zonal electric field response.

Interestingly, previous studies on solar quiet currents during SSW events have not consider the application of chaos theory. This study aims to bridge this gap by investigating the chaotic behavior of the solar quiet current system in response to SSW effects over the European and African sectors. To examine the ionosphere during 2009 and 2021 SSW events, this study utilizes a robust methodology combining two innovative techniques: the Horizontal Visibility Graph (HVG), rooted in graph theory, to preprocess solar quiet current time series data, and Fuzzy Entropy (FuzzyEn) analysis to reveal the underlying chaotic behavior in the ionosphere during SSW. The reason why this study considers the combination of HVG and Fuzzy Entropy techniques is that Fuzzy Entropy is indeed robust to small-amplitude noise, some subtle features in the solar quiet current time series may still be obscured if we rely on FuzzyEn alone. The HVG transformation helps by emphasizing the "visibility" relations between data points effectively highlighting structural patterns that may be drowned out in the raw time series. In addition, when FuzzyEn is computed on node-degree sequence (complex network representation), it often provides clearer differentiation of regimes or subtle changes in the system that might otherwise remain hidden. Thus, the combined HVG and FuzzyEn approach can yield features more robust to measurement noise and more sensitive to underlying structural variations in the solar quiet current.

1.1 Characterization of 2009 and 2021 Major SSW Events

The 2009 SSW event occurred from January to March. Its rising stratospheric temperature and the corresponding stratospheric zonal mean wind was categorized into six phases during these periods: SSW Pre-Condition Phase, SSW Ascending Phases, SSW Peak Phase, SSW Descending Phase,

121   After SSW Phase, and No SSW phase (Figure (1)). The red color represents the stratospheric mean

122   air temperature (k) at 10hPa. While the black color is the stratospheric zonal mean wind at 10hPa.

123
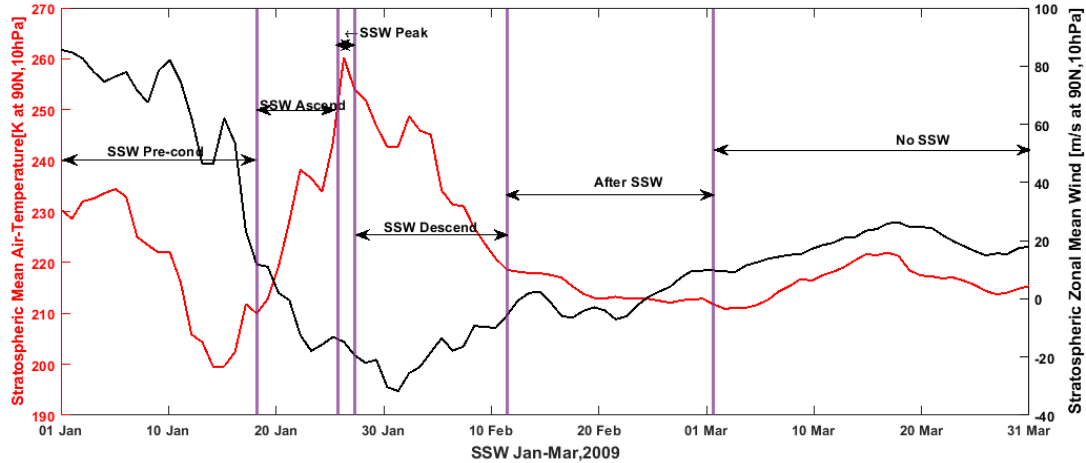
124   Figure 1: The stratospheric zonal mean air temperature and zonal mean wind occurring January-

125   March, 2009 showing the SSW Precondition Phase, SSW Ascending Phase, SSW peak Phase,

126   SSW Descending Phase, After SSW Phase and no SSW phase. The stratospheric parameter during

127   the 2009 SSW event is obtained from the National Oceanic and Atmospheric Administration

128   (NOAA).

129   The SSW precondition phase represents the start of the increase in the stratospheric temperature

130   (1-16 January) shown in Figure 1, the SSW ascending phase signifies when the stratospheric

131   temperature increases (17-21 January), the SSW peak phase is when the stratospheric temperature

132   reaches its maximum (22-24 January), the SSW Descending phase indicates the begin of the

133   stratospheric temperature decline (25 January-12 February), the After SSW phase represents when

134   the stratospheric temperature begins to recover to its normal state (13 February-2 March), and the

135   No SSW phase represents when the stratospheric temperature finally recovers to its normal state

136   (3-31 March). The SSW event was categorized in accordance to the work of (Bolaji et al., 2016b).

137   The stratospheric temperature and its corresponding zonal mean wind for the 2021 SSW event is

138   shown in Figure 2. The SSW occurred from December 2020 to February 2021 and was also

139   categorized into six phases. The SSW precondition phase spans between 1 and 27 December, 2020,

140   the SSW ascending phase is from 28 December 2020 to 2 January 2021, while the SSW peak phase

141   ranges from 3-5 January 2021, the SSW descending phase spans within 6-14 January 2021, and

142   the After-SSW phase is from 15 January-16 February 2021. Finally, the No SSW phase emerges

143   from 17-28 February 2021.

144
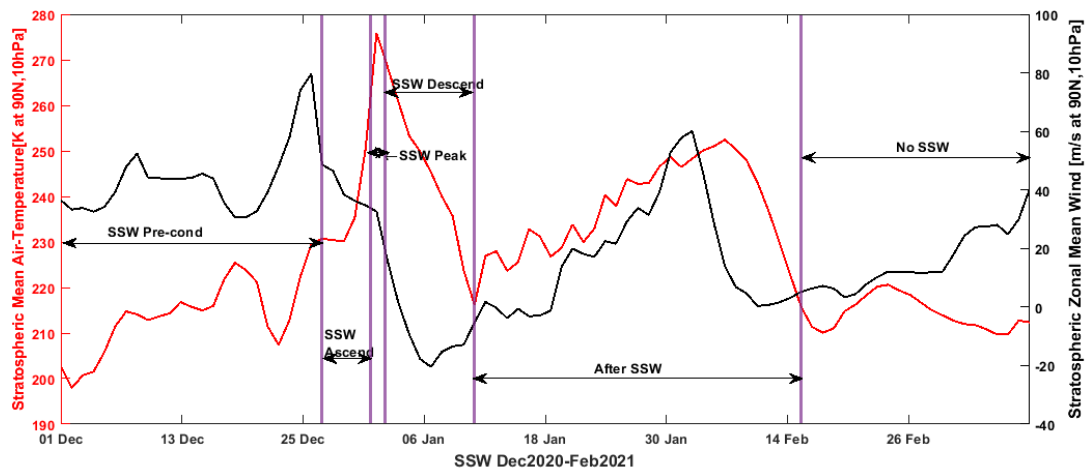
145   Figure 2: The stratospheric zonal mean air temperature and zonal mean wind from December 2020

146   until February, 2021 revealing the SSW Precondition Phase, SSW Ascending Phase, SSW peak

147   Phase, SSW Descending Phase, After SSW Phase and no SSW phase. The stratospheric parameter

148   during the 2021 SSW event is obtained from the National Oceanic and Atmospheric

149   Administration (NOAA).

150   **1.2 Global Scale of geomagnetic activities during the 2009 and 2021 SSW Events**

151   The year 2009 was the beginning of a solar minimum of the solar cycle 24 while the year 2021

152   was the end of solar minimum in the solar cycle 24. Generally, solar minimum years are periods,

153 where the geomagnetic disturbances mostly record quiet days. This indicates that the years 2009

154 and 2021 of solar cycle 24 are periods where the geomagnetic disturbances were minimal. The

155 planetary index (K_p) and the solar flux activity during the months of 2009 and 2021 SSW event

156 are shown in Figures (3 & 4) respectively. During the 2009 SSW event (January-March), the

157 planetary K_p index generally depicts quiet geomagnetic conditions ($K_p \leq 3$) for most days, as

158 shown in Figure 3. However, there were 11 exceptions (January 3, 19, 26, February 4, 14-15, 25,

159 28, March 13, and 24) where K_p index values exceeded 3, indicating geomagnetic disturbance.

160 These days were excluded from the SSW characterization to maintain a focus on quiet geomagnetic

161 periods.

162 .
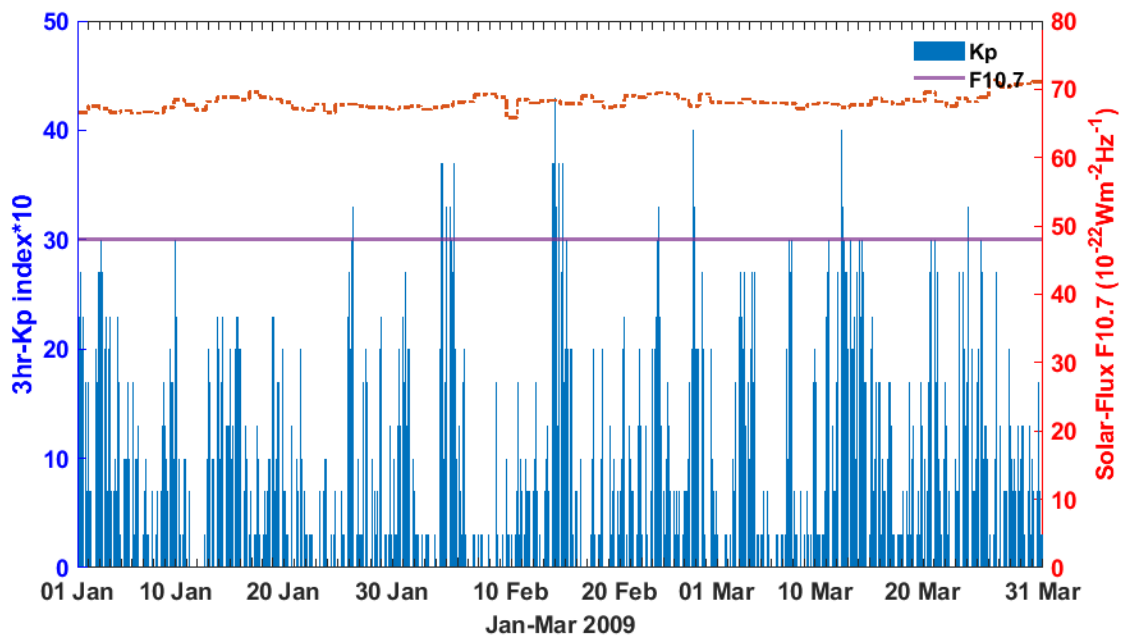
163 Figure 3: The planetary index K_p (blue bars) and Solar flux $F_{10.7}$ (red lines) between January to

164 March, 2009. The planetary (K_p) and Solar flux activity ($F_{10.7}$) during 2009 SSW periods collected

165 from the Space Physics Data Facility, NASA

166   The planetary K_p index during the 2021 SSW event (December 2020 to February 2021), as shown

167   in Figure 4, generally indicated quiet geomagnetic conditions ($K_p \leq 3$) for most days and the solar

168   flux activity was within $F_{10.7} \sim 100$. However, elevated K_p index values (> 3) were observed on 17

169   specific days (Dec 10, 21, 23, Jan 5, 6, 11, 24, 25, 27, Feb 2, 6, 12, 16, 20, 22, 23), which were

170   excluded from the analysis to focus on geomagnetically quiet periods.

171   A comparative analysis of the day-to-day geomagnetic activity in January-March, 2009 and

172   December 2020-February 2021 SSW events reveals that most days during these periods manifest

173   K_p index values ≤ 3, indicating minimal geomagnetic activity. This observed space weather feature

174   underscores the uniqueness of the selected SSW events for this study. An investigation into the

175   chaotic behavior of the ionosphere during periods of low geomagnetic activity of SSW will reveal

176   the significant impact of SSW events on ionospheric dynamics within the European and African

177   sectors.

178
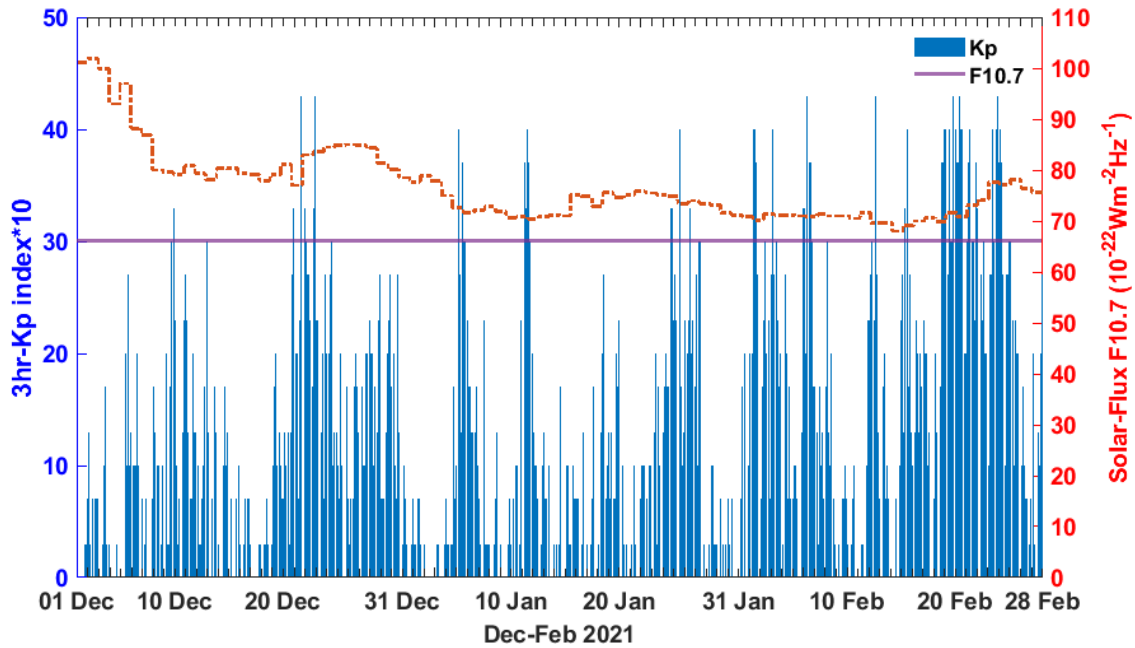
179   Figure 4: The planetary index: K_p (blue bar) and Solar flux F$_{10.7}$ (red lines) from December 2020-

180   February, 2021. The planetary (K_p) and Solar flux activity ($F_{10.7}$) during 2021 SSW periods

181   collected from the Space Physics Data Facility, NASA

182   **2. Data Acquisition and Method of Analysis**

183   The ground-based magnetometer data acquired from the Magnetic Data Acquisition System

184   (MAGDAS) at the International Research Centre for Space and Planetary Environment Science

185   ($i - SPES$), Fukuoka, Japan (http://magdas2.serc.kyushu-u.ac.jp/) was used in this study. The

186   geographical location of the studied areas is shown in Figure 5.

187
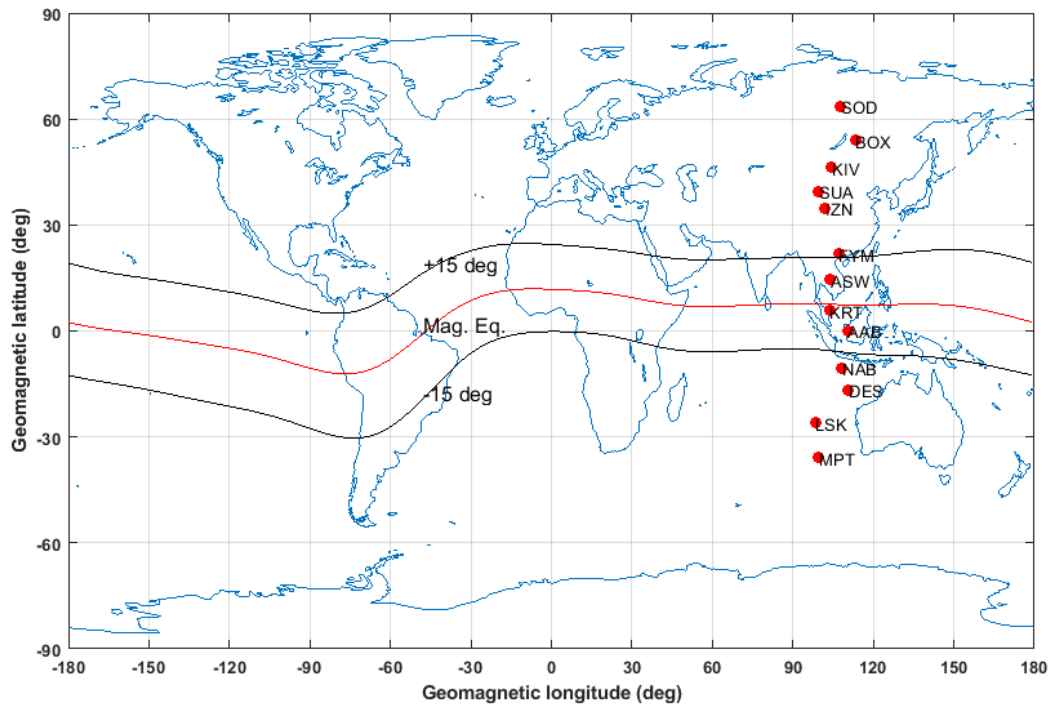
188   Figure 5: The geomagnetic location of the magnetometer observatories stations investigated across

189   the Europe and Africa sector.

190   The acquired magnetic data from MAGDAS covers 8 magnetometer stations situated in the Africa

191   sector distributed within the geographical latitudes of both Northern and Southern Hemisphere

192   shown in Table 1. The geomagnetic coordinate reference year for the stations listed in Table 1 is

193   2009.

194   **TABLE 1: STATIONS INVESTIGATED ACROSS EUROPE AND AFRICA SECTOR**

S/No	Stations	Country	Geographical latitude	Geographical Longitude	Geomagnetic Latitude	Geomagnetic Longitude	Local Time (LT)	Magnetometer Network
1	Sodankyla (SOD)	Finland	67.37	26.63	63.70	107.68	UTC+3	INTERMAGNET
2	Borok (BOX)	Russia	58.07	38.23	53.92	113.32	UTC+3	INTERMAGNET
3	Kiev Dymer (KIV)	Ukraine	50.70	30.30	46.32	104.39	UTC+3	INTERMAGNET
4	Surlari (SUA)	Romania	44.68	26.25	39.52	99.52	UTC+3	INTERMAGNET
5	Iznik (IZN)	Turkey	40.50	29.72	34.74	102.13	UTC+3	INTERMAGNET
6	Fayum (FYM)	Egypt	29.18	35.50	21.78	106.00	UTC+2	MAGDAS
7	Aswan (ASW)	Egypt	23.50	32.51	14.56	103.89	UTC+2	MAGDAS
8	Khartoum (KRT)	Sudan	15.33	32.32	5.69	103.80	UTC+2	MAGDAS
9	Addis Ababa (AAB)	Ethiopia	9.01	38.74	0.14	110.44	UTC+3	MAGDAS
10	Nairobi (NAB)	Kenya	-1.10	36.48	-10.58	108.18	UTC+3	MAGDAS
11	Dar es Salaam (DES)	Tanzania	-6.80	39.28	-16.62	110.72	UTC+3	MAGDAS
12	Lusaka (LSK)	Zambia	-15.23	28.19	-26.06	98.31	UTC+2	MAGDAS
13	Maputo (MPT)	Mozambique	-25.50	32.36	-35.92	99.56	UTC+2	MAGDAS

195

196   Also, magnetometer stations in the Europe were acquired from the International Real-time

197   Magnetic Observatory Network (INTERMAGNET), available online at www.intermagnet.org.

198   The collection consists of 5 magnetometer observatory stations across Europe, see Table 1. The

199   magnetometer data were acquired during the periods of the 2009 and 2021 SSW events. Owing to

200   lack of magnetic data at geographical longitude between 26^0 and 40^0 in Africa sector, during 2021

201   SSW, our study of 2021 SSW was restricted only to European sector.

202   The planetary (K_p) index during 2009 and 2021 SSW periods was downloaded from GFZ Indices

203   of Global Geomagnetic Activity (https://www.gfz-potsdam.de/Kp-index/) while the Solar flux

204 activity ($F_{10.7}$) at 2009 and 2021 SSW periods were collected online from the archive of the Space

205 Physics Data Facility, NASA (https://omniweb.gsfc.nasa.gov/form/dx1.html).

206 The daily mean values of zonal mean air temperature and wind during the periods of 2009 and

207 2021 SSW were acquired from the National Oceanic and Atmospheric Administration (NOAA)

208 (https://psl.noaa.gov/data/getpage/). The solar quiet currents, $S_q(H)$, was derived using the H-

209 component of the magnetic field data with daily resolution (with time unit in minutes). A magnetic

210 field model (CHAOS-8.1), spanning 1999-2025, was obtained from DTU Space

211 (https://www.space.dtu.dk/english/research/scientific_data_and_models/magnetic_field_models)

212 to determine the ionospheric field. CHAOS-8.1 is derived from magnetic field observations by

213 low-Earth orbiting satellites (Swarm, MSS-1, CSES, CryoSat-2, CHAMP, SAC-C, and Ørsted)

214 and ground observatory measurements.

215 2.1 Derivation of Solar quiet Current $S_q(H)$ time Series

216 To derive the day-to-day $S_q(H)$ current time series, magnetic field data from various magnetometer

217 stations across European and Africa sector were archived. We focus on acquiring magnetic field

218 data from the magnetometer stations that are situated within the geographical longitude (26°-40°).

219 Some of the acquired magnetic data, especially the stations in Europe sector are provided in

220 Cartesian (X, Y, Z) coordinate system, and was converted to geomagnetic (H, D, Z) coordinate

221 system using Rotation Matrix method (Barton and Tarlowski, 1991). We applied a magnetic field

222 model (CHAOS-8.1) with the acquired magnetic field data to obtain the ionospheric field. The H-

223 component of the magnetic field model (CHAOS) was subtracted from the H-component of the

224 acquired magnetic data.

225
$$\Delta H = \Delta H_{magnetic\ data} - \Delta H_{model} \qquad (1)$$

226   To minimize the disturbance field arising from the magnetospheric currents (Bolaji et al., 2016b).

227   The values of the geomagnetic storm index in minutes (SYM-H) were subtracted from the H-

228   component (ΔH).

229
$$\Delta H_{local} = \Delta H - (SYM - H \times \cos(L)) \qquad (2)$$

230   To estimate the solar quiet current $S_q(H)$ time series, the average nighttime values (in minutes) of

231   the H-component between 24:00 and 1:00 local time (LT) for a particular day refers as Baseline

232   Value (BLV) was estimated using equation (3).

233
$$BLV = \frac{\Delta H_{24} + \Delta H_{01}}{2} \qquad (3)$$

234   The notation ΔH_{24} and ΔH_{01} are the 60 minutes values of H component at 24:00 and 01:00 LT

235   respectively. Where BLV represent the Baseline line value. The residual value after subtracting the

236   baseline value from the H-component gives rise to the solar quiet current time series.

237
$$S_q(H) = \Delta H_{local} - BLV \qquad (4)$$

238   Where $S_q(H)$ is the solar quiet current considered in minutes. The analysis of the $S_q(H)$ was

239   deduced for all the day-to-day activities of the 2009 SSW (January-March) and 2021 SSW

240   (December 2020-Februay) periods for all stations under investigation.

241   **2.2 Detrending of Solar quiet Sq(H) Current Time Series by Horizontal Visibility Graph**

242   **(HVG).**

243   The time series of the solar quiet current. Sq(H) derived during the periods of the 2009 and 2021

244   SSW was subjected to the HVG method which transform the series into a complex network. The

245   calculations were performed using the ts2vg Python module, specifically utilizing the

246   HorizontalVG class, which represents one of the types of visibility graphs, namely the 'Horizontal

247 Visibility Graph'. The input to this process is a time series, which is transformed into a network

248 where each point in the series becomes a node, and edges are formed based on the visibility criteria

249 between points (Conejero et al., 2024; Gonçalves et al., 2016; O'Pella, 2019; Luque et al., 2009;

250 Zou et al., 2019). By applying this method, we calculate the degree (number of connections) for

251 each point in the time series, capturing the number of other points it can 'see' in the horizontal

252 visibility graph. The output is a list of degrees for each point, reflecting the local connectivity

253 structure within the time series, which helps reveal patterns, dependencies, and variability within

254 the data. The HVG is mathematically described as follows:

255 Let us consider a time series of N-data points be represented as:

256
$$[x_i, i = 1,2, \dots, N] \qquad (5)$$

257 Two nodes i and j in the graph are connected, if it is possible to trace a horizontal line in the series

258 linking x_i and x_j not intersecting intermediate data height, fulfilling:

259
$$x_i, x_j > x_n \text{ for all } i < n < j \qquad (6)$$

260 **2.3 Fuzzy Entropy (FuzzyEn)**

261 Fuzzy entropy (FuzzyEn) is a powerful and popular nonlinear tool used to assess the dynamical

262 characteristics of time series data (Ishikawa and Mieno, 1979; Li et al., 2017; Azami et al., 2019;

263 Chen et al., 2007). It provides a quantitative measure of a signal's complexity and chaos. High

264 entropy indicates a more irregularity (chaotic) dynamics, whereas low entropy suggests a more

265 regular or periodic nature. FuzzyEn was developed to overcome the shortcoming of approximate

266 entropy (ApEn) and sample entropy (SampEn) (Azami et al., 2019; Li et al., 2017; Dass et al.,

267 2019). FuzzyEn uses exponential functions with Fuzzy boundaries. It is expressed mathematically

268   as follows. Given a time series, we embed it using a given embedding dimension (m). Then, a

269   new m-dimensional vector (X_m) is formed as

270
$$X_m(i) = [X_i, X_{i+1}, ..., X_N] - x0_i \qquad (7)$$

271   These vectors represent m consecutive x-values, starting with the i-th points, and with the baseline

272      $x0_i = \frac{1}{m}\sum_{j=0}^{m-1} x_{i+j}$ removed. Then, the distance between vectors $X_m(i)$ and $X_m(j)$, $d_{i,j,m}$ can be

273   defined as the maximum absolute difference between their scalar components. Given n and r, the

274   degree of similarity $(D_{i\ j,m})$ of the vectors $X_m(i)$ and $X_m(j)$ is calculated using the fuzzy function:

275
$$D_{i,j,m} = \mu(d_{i,j,m}, r) = exp\left(\frac{-(d_{i,j,m})^n}{r}\right) \qquad (8)$$

276   Where n and r are the FuzzyEn power and threshold respectively. The function ϕ_m is defined as

277
$$\phi_m(n,r) = \frac{1}{N-m}\sum_{i=1}^{N-m}\left(\frac{1}{N-m-1}\sum_{\substack{j=1 \\ j \neq i}}^{N-m} D_{i,j,m}\right) \qquad (9)$$

278   Repeating the same procedure from equation (7) and equation (8) for the vector $X_{m+1}(j)$, i.e., for

279   dimension $(m+1)$, the function ϕ_{m+1} is obtained. Therefore, FuzzyEn can be estimated as

280
$$\text{FuzzyEn}\ (m,n,r,N) = \ln \phi_m(n,r) - \ln \phi_{m+1}(n,r) \qquad (10)$$

281   In this study, we applied the HVG and FuzzyEn to the solar quiet current, Sq(H), to investigate

282   ionospheric chaos during SSW across the Europe and Africa sector. The computational parameters

283   used for FuzzyEn analysis included an embedding dimension $(m = 1)$ and a tolerance threshold

284   defined as r_1=0.2×std, where std represents the standard deviation of the time series X.

285   Additionally, the argument exponent (pre-division) r_2=3 was applied, along with a time delay of

286   τ=1. The window size used for the analysis was s=200.

287 The calculations were performed using Python with the EntropyHub library [EntropyHub. An

288 Open-Source Toolkit for Entropic Time Series Analysis. Available online:

289 https://www.entropyhub.xyz/ (accessed on 27 February 2024).] (version 0.2), which provides a

290 reliable and standardized method for calculating FuzzyEn, ensuring that the results can be

291 compared across different studies. EntropyHub integrates many established entropy methods into

292 a single package, available for Python, MatLab, and Julia users. By utilizing this library, we

293 ensured the consistency and reproducibility of our entropy calculations.

294 The solar quiet current time series during the SSW periods of 2009 (January-March) and 2021

295 (December 2020-February 2021) was transformed via the Horizontal Visibility Graph (HVG) to

296 obtain a complex network representation. From this network, we derive a new node-degree time

297 series (maintaining the same length as the original). We then apply a sliding-window approach to

298 calculate the Fuzzy Entropy on this new node-degree time series. Thus, while the HVG step

299 converts the solar quiet current time series into a graph, the FuzzyEn measure is ultimately

300 computed on the node-degree time series derived from that graph.

301 **3. Observation and Results**

302 A sample of solar quiet current $S_q(H)$ on 31st of March 2009 at Addis Ababa, Ethiopia is shown

303 in Figure 6 (a-d). The panel (a) represents the time series of the solar quiet current derived in

304 minutes. While the Horizontal Visibility Graph (HVG) step indeed yields a graph (i.e., a complex

305 network) of the solar quiet current time series, we subsequently derive a new time series from this

306 network (e.g., by taking the node degrees). Panel (b) present node degree values of the HVG, and

307 by this it is some kind of detrending, effectively reflecting the node-degree sequence derived from

308 the solar quiet time series data, which preserves the same length as the original time series. The

309 panel (c) is the FuzzyEn depicting the entropy of the solar quiet current without applying HVG

310 transformation. The result in panel (d) depicts the values of Fuzzy Entropy for the node degree

311 distribution of this network representation for solar quiet current. We notice that the solar quiet

312 current time series in panel (a) depicts an enhancement in magnitude during the peak noon periods

313 in its daily variation, while at pre-noon and post-noon periods, a gradual increment and a decrease

314 in the magnitude of the solar quiet current was observed. The results of the Fuzzy Entropy for the

315 detrended time series obtained after HVG transformation reveals a gradual decrease in entropy at

316 noon-periods. While, at pre-noon and post-noon periods, the entropy depicts an increment. The

317 detrended solar quiet current time series resulting from the HVG transformation highlight distinct

318 entropy changes. These approach captures peaks and troughs in the time series of solar quiet

319 current through horizontal visibility, thereby unveiling subtle fluctuations in the dynamical

320 behavior of the ionospheric current system. When FuzzyEn is low, it typically suggests more

321 orderliness (less chaotic) behavior, whereas higher FuzzyEn values are associated with greater

322 complexity or chaos. With this viewpoint, the HVG and FuzzyEn combination appears to reveal

323 dynamical characteristic of the solar quiet current, including the potential emergence of chaotic

324 behavior during the 2009 (January–March) and 2021 (December 2020–February 2021) SSW

325 events.

326 The day-to-day latitudinal distribution of entropy across Europe and Africa sector in January 2009

327 is shown in Figure 7. The result depicts the entropy changes in color representation. The yellow

328 color revealing the ranges of Fuzzy Entropy values between 1.2 and 1.4 indicates high entropy.

329 This high entropy signifies the presence of ionospheric chaos in the ionospheric current system.

330 The light blue color ranging at approximately 0.8~1.2 reveals a declining entropy value which

331 indicates a transition from chaos to orderliness behavior in the ionospheric current system. While

332 the deep blue color ranging at 0.6~0.8 depicts low entropy values. The low entropy reveals the

333 presence of orderliness behavior in the ionospheric current system. We noticed that in the day-to-

334 day latitudinal distribution of entropy across the stations in the European and African sector. Some

335 days in January 2009 depicts the presence of ionospheric chaos at most of the stations shown in

336 Figure 7. High entropy values were observed at stations situated at IZN, SUA, KIV, BOX and SOD

337 on 1st, 4th, 8th, 10th, 14th, 18th-25th, and 28th-29th of January 2009. On 25th of January, a higher

338 entropy values were depicted across all the stations in Europe and Africa sector. This observed

339 feature of high entropy unveils the presence of chaotic behavior in the ionospheric dynamics of

340 Europe and Africa sector. Low entropy values, signifying orderliness behavior in the dynamics of

341 ionosphere was observed on 2nd, 5th, 7th, 9th, 11th-13th, 15th-16th, 20th, 23rd-24th, 27th and

342 30th-31st of January. This observed low entropy are mostly domiciles in the Africa sector. In

343 addition, our analysis revealed that lower entropy values were found on 13th and 15th of January

344 spreading across stations in Europe and Africa sector. This observed feature of low entropy across

345 Europe and Africa sector reveals that the dynamics of the ionosphere on 13th and 15th of January

346 exhibits a highly orderliness behavior.

347 We display the contour plots of the day-to-day latitudinal distribution of entropy on February 2009

348 in Figure 8. The changes in entropy depicts high values of Fuzzy Entropy revealing the presence

349 of ionospheric chaos. This trend of high entropy values was noticed on 1st-2nd, 9th-10th, 17th of

350 February signifying that the ionospheric dynamics of the aforementioned days are associated with

351 chaotic behavior. In addition, 1st and 17th February exhibited a higher chaotic behavior that spread

352 across all the stations investigated. This observation further strengthening the evident influence of

353 SSW effects on the ionospheric dynamics on these dates. Notably, low entropy implying the

354 presence of orderliness behavior in the dynamics of the ionosphere was obvious on 5th-8th, 11th-

355 16th, 18th-2th of February 2009. However, 5th and 20th of February exhibited the lowest entropy

356 values, revealing that the state of the ionosphere is exhibits strong orderliness behavior.

357 The day-to-day latitudinal distribution of entropy across the European and African sector on March

358 2009 is shown in Figure 9. Most of the Fuzzy entropy values are associated with low entropy. For

359 instance, 1st-6th, 8th-18th, 20th-23rd, 25th-28th, and 31st of March depicts low changes in entropy

360 in most of the stations. High entropy values associated with the presence of ionospheric chaos

361 were found on 7th, and 29th-30th of March.

362 In 2021 SSW event analysis, because of unavailability of magnetic data in Africa sector especially

363 in stations situated with the geographical longitude of $(26^0 - 40^0)$. Our analysis during 2021 SSW

364 was restricted to only European sector. The result of the day-to-day latitudinal distribution of

365 entropy across European sector is presented in Figure 10. We observed that the changes in entropy

366 from 1st to 6th of December at the SOD, BOK and KIV stations reveals a consistently low entropy

367 values, indicating that the state of the ionosphere at these stations exhibits a consistent orderliness

368 behavior during these periods. However, at SUA and IZN, a consistent high entropy values

369 indicating the presence of ionospheric chaos was observed from 1st to 5th of December 2020. The

370 day-to-day entropy changes on 7th-9th, and 11th-20th of December at SOD, BOX and KIV depicts

371 a consistent high value of Fuzzy Entropy. Interestingly, SUA and IZN were consistently associated

372 with a low entropy distribution from 8th to 22nd of December. This observed consistent feature of

373 low entropy at SUA and IZN signifies that the influence of SSW effects on regional ionosphere of

374 SUA and IZN manifest an orderliness behavior in the underly dynamics of ionosphere at this

375 region. Furthermore, the possible emergence of ionospheric disturbances at SUA and IZN during

376 those observed days highlights that perturbation due to 2021 SSW effect is minimal. A consistent

377 decline feature from chaotic to orderliness behavior in the ionospheric dynamics was observed

378   also at SOD, BOK, and KIV from 25th to 31st of December 2020, while SUA and IZN exhibited

379   some features of ionospheric chaos on 30th and 31st of December.

380   For SSW of January 2021, the day-to-day latitudinal distribution of entropy across Europe sector

381   is displayed in Figure 11. The latitudinal distribution depicts low entropy across the day-to-day

382   observation in January. For instance, 1st-6th, 8th, 9th-10th, 13th-17th, 19th-23rd, 28th-29th and

383   30th-31st of January reveals low entropy values across the stations investigated in the Europe

384   sector implying that the ionosphere at this region exhibits orderliness behavior in its underlying

385   dynamics in most of the days consider in this study. Notably, high entropy, indicating the presence

386   of ionospheric chaos was observed at SUA and IZN on 4th, 7th, 10th, 12th, and 13th of January

387   2021. In Figure 12 we depicted the day-to-day latitudinal distribution of entropy in February 2021

388   across Europe sector. The changes in entropy reveal high entropy, suggesting the presence of

389   ionospheric chaos on 9th, 12th, 16th-18th, 21st, and also from 24th to 27th of February 2021 at

390   SOD, BOX, SUA and IZN. In contrast, KIV consistently exhibited low values of entropy from 1st

391   to 8th of February.

392   **3.1 Ionospheric Chaos During Phases of 2009 SSW**

393   Display in Figure 13 is the latitudinal distribution of entropy across Europe and Africa sector

394   during different phases of 2009 SSW. The entropy analysis during the precondition phase of SSW

395   depicts high entropy values across the stations in the European sector signifying that the

396   precondition phase of 2009 SSW were associated with the emergence of ionospheric chaos. The

397   observed features of high entropy values unveiling pronounced ionospheric chaos is found at SUA,

398   KIV, BOX and SOD. This observation further reveals that the influence of SSW effects introduces

399   an emergence of ionospheric perturbation in SUA, KIV, BOX and SOD at the preconditioning

400   phase of 2009 SSW in Europe sector. It is noteworthy that the period from January to March 2009

401   were strongly associated with minimal activities of geomagnetic disturbance (see, Figure 2a). In

402   the African sector, we noticed that the SSW preconditioning phase is characterized by a declining

403   and low entropy values, implying that the regional ionosphere across Africa sector is revealing a

404   suppression of orderliness behavior in the ionospheric dynamics at the preconditioning phase of

405   2009 SSW. A low entropy was seen at AAB, NAB and DES during the preconditioning phase

406   signifying that the underlying dynamics of the ionosphere at AAB, NAB, and DES are exhibiting

407   orderliness behaviour as the preconditioning phase of SSW emerges.

408   During the ascending phase of SSW, we observed also a low entropy values at stations in Africa

409   sector up to IZN. However, high values of entropy implying the presence of ionospheric chaos

410   were noticed at KIV, BOX, and SOD. The high entropy observed at KIV, BOX, and SOD during

411   the ascending phase signifies that the influence of SSW effect on the regional ionosphere at KIV,

412   BOX, and SOD is eminent. This suggests that SSW events significantly affect ionospheric

413   dynamics, leading to an increased chaotic pattern across Europe sector during the ascending phase

414   of 2009 SSW. In the African sector, we observed that the region depicts low entropy values during

415   ascending phase. This further signifies that the regional ionosphere in the Africa sector

416   demonstrates orderliness behavior at the ascending phase of SSW.

417   During the peak phase of SSW 2009, evidence of ionospheric chaos was obvious at SOD, BOX,

418   KIV, and SUA. The changes in Fuzzy entropy during this peak phase depicts high values,

419   indicating significant disturbances in the ionosphere at Europe sector. A feature of declining

420   entropy value was noticed to spread from IZN to DES. However, at around 4-10LT, low entropy

421   values were seen at KRT, AAB and NAB. This observed declining entropy with a little feature of

422   low entropy at KRT, AAB and NAB reveals that the regional ionosphere in Africa sector during

423   the peak phase of SSW experience a suppression of orderliness behaviour. The suppression in

424   orderliness behavior as SSW peak phases emerges further suggest that the regional ionosphere of

425   Africa sector also experience a chaotic behavior. However, the European sector during the peak

426   phase depict higher degree of chaotic behavior. We suspect that the emergence of chaotic behavior

427   due to SSW effect in Africa sector results in the suppression of orderliness behaviour.

428   At the descending phase of SSW, high entropy values associated with the presence of ionospheric

429   chaos was evident at SOD, BOX, KIV, SUA, IZN. However, FYM, ASW, KRT, DES, LSK, and

430   MPT reveals a declining entropy value, while AAB and NAB at around 8-16LT of the descending

431   phase of SSW depicts low entropy values. The observed feature of declining entropy during the

432   descending phase at stations situated in Africa sector signifies that the ionospheric dynamics

433   exhibits a suppression in orderliness behaviour. This suppression of orderliness further suggests

434   that the SSW effects during the descending phase introduce perturbation into regional ionosphere

435   of Africa resulting to the suppression of orderliness behavior.

436   The after-SSW phase of 2009 also demonstrates a distribution of high values of entropy at SOD,

437   BOX, KIV, SUA, SUA, and FYM. In the stations situated in Africa sector, low entropy begins to

438   spreads from AAB to LSK while ASW, KRT and MPT depicts a declining value of entropy. The

439   observed entropy changes during After-SSW phase signifies that SSW induced effect on Africa

440   regional ionosphere begins to reduce. During the no-SSW phase, the degree of entropy associated

441   with ionospheric chaos suppress at the following stations SOD, BOX, KIV, SUA and IZN. While

442   a steady low entropy value was seen around ASW, KRT, AAB, NAB, DES, LSK, and MPT

443   stations. This steady low entropy features seen during the no-SSW phase reveals that the regional

444   ionosphere of Africa sector recovers back to its original dynamics.

445

3.2 Ionospheric chaos during phases of 2021 SSW

Shown in Figure 14 is the 2021 SSW latitudinal distribution of entropy across Europe sector at precondition, ascending, peak, descending, After-SSW and no-SSW phases. The Precondition phase at SOD, BOX, and KIV depicts high values of entropy signifying that ionospheric chaos is dominant during this period, while a declining and low entropy change was observed at IZN and SUA. The ascending, peak, descending and after SSW phases exhibit a consistent low entropy value in their latitudinal distribution, suggesting orderliness behavior in the ionosphere across SOD, BOX and KIV. In contrast, at SUA a consistent increase in entropy was evident. This consistent increase in entropy at SUA during all the phases of SSW implies that the ionospheric dynamics is consistently exhibiting chaotic behavior due to the influence of SSW.

4. Discussion of Results

The results unveil the dynamical characteristic in the solar quiet current $S_q(H)$ system during the 2009 and 2021 SSW events. Employing Horizontal Visibility Graph (HVG) and Fuzzy Entropy analysis, this study quantifies the chaotic and orderliness behavior exhibited by the ionospheric current system during SSW events across the European and African sectors. Ionospheric chaos is found to be most pronounced at European sector stations, particularly SUA, KIV, BOX, and SOD, demonstrating a higher degree of complexity and unpredictability in the ionospheric dynamics at this location. A notable dynamical feature of the ionospheric current system within the African sector was the consistent low entropy values observed at AAB, NAB, and DES, indicating the presence of orderliness behavior. In addition, our analysis revealed a transition from chaotic to orderliness behavior in the African sector as the stratospheric warming intensified. This transition was accompanied by a decline in entropy values. For instance, during the preconditioning phase of 2009 SSW, our results showed a decline in entropy values, signifying a shift towards orderliness

469   behavior. Specifically, FYM, ASW, KRT, DES, LSK, and MPT exhibited declining entropy values,

470   while AAB and NAB showed low entropy values around 9-11 LT. This decline in entropy during

471   the preconditioning phase suggests that the SSW effects introduce perturbation to the regional

472   ionosphere of the African sector, leading to a suppression of chaotic behavior, and transit to

473   orderliness behavior in Africa sector. The European sector stations, comprising SOD, BOX, KIV,

474   SUA, and IZN, exhibited elevated entropy values, signifying the presence of pronounced

475   ionospheric chaos at preconditioning phase. During the ascending phase of the 2009 SSW, our

476   analysis revealed that the European sector stations (SOD, BOX, KIV, SUA, and IZN) consistently

477   exhibited high entropy values, indicating the presence of chaotic behavior. This pronounced

478   ionospheric chaos suggests that the SSW-induced effects on the regional ionosphere of the

479   European sector are particularly significant. By comparison, the African sector exhibited more

480   variable entropy measures, fluctuating between declining and low entropy values. Notably, Africa

481   stations comprising of FYM, ASW, KRT, AAB, NAB, DES, LSK, and MPT showed low entropy

482   values between 8-12 LT, while declining entropy values were observed at other local times. This

483   divergence suggests that the ionosphere in the African sector are becoming more synchronized to

484   orderliness behavior as the stratospheric temperature rises.

485   At the peak phase of 2009 SSW, our findings reveal an extended feature of converging orderliness

486   behavior in the African sector. Notably, declining entropy values were observed at FYM, ASW,

487   KRT, DES, LSK, and MPT, while low entropy values were evident at AAB and NAB. This

488   converging orderliness behavior in the African sector during the SSW peak phase suggests that an

489   external perturbation, induced by SSW effects, is influencing the regional ionosphere. This

490   perturbation appears to suppress the chaotic behavior of the ionospheric current system in the

491   African sector. Meanwhile, stations in the European sector, including SOD, BOX, KIV, and SUA,

continued to exhibit chaotic behavior in their regional ionospheric dynamics. The descending phase of 2009 SSW, reveals a gradual recovery to orderliness behavior in the African sector. Low entropy values were evident, indicating a return to orderliness dynamics in the regional ionosphere. The recovery was characterized by low entropy values at KRT, AAB, NAB, and DES, while other African sector stations exhibited declining entropy values. This observed entropy distribution during the SSW's descending phase suggests that the African sector's regional ionosphere is reverting to orderliness behavior. Conversely, European sector stations, including IZN, SUA, KIV, BOX, and SOD, consistently displayed chaotic behavior.

During the after-SSW phase, a notable decline in entropy was observed at FYM, ASW, KRT, LSK, and MPT, implying a transition towards orderliness behavior at these stations. Additionally, low entropy values were recorded from AAB to DES, signifying that ionosphere at AAB, NAB, and DES exhibiting orderliness behavior. On the other hand, European sector including SOD, BOX, KIV, SUA, and IZN continued to exhibit high entropy values suggesting a persistent ionospheric chaos. At the no-SSW phase, a notable expansion and spread of low entropy values were observed across all stations in the African sector. This entropy distribution pattern indicates that the regional ionosphere has fully recovered and the dynamics is reverted to orderliness behavior.

In the 2021 SSW, entropy analysis revealed distinct patterns of ionospheric chaos and orderliness across different stations. Initially, chaos increased at KIV, BOX, and SOD during the preconditioning phase, while SUA and IZN exhibited orderly behavior. In contrast, SOD, BOX, and KIV showed orderly behavior during the ascending, peak, and descending phases. However, chaos re-emerged at these stations during the after-SSW and no-SSW phases. Notably, SUA exhibited prominent chaotic behavior throughout the ascending, peak, descending, after, and no-

514 SSW phases, highlighting the significant influence of SSW on ionospheric dynamics in certain

515 regions of the European sector.

516 These findings of ionospheric chaos in most of the stations situated in the Europe sector reveals

517 the evidence that the 2009 SSW effect indeed significantly influenced the ionospheric dynamics

518 in European sector. Interestingly, during the 2009 SSW periods, the daily geomagnetic activities

519 were mostly characterized by a planetary index of $K_p \leq 3$ and those days whose K_p index value

520 exceed 3 was discarded in the analysis. While the solar flux ($F_{10.7}$) was approximately 72 (see

521 Figure 3). This geomagnetic index record signifies that geomagnetic disturbances were extremely

522 low during the 2009 SSW. Therefore, the finding that ionospheric chaos been dominant in most

523 stations located in the European sector provides additional evidence of the SSW's effect on the

524 regional ionosphere in Europe sector. The presence of ionospheric chaos could result to the

525 formation of large disturbances in the European sector owning to the impact of disruption on

526 communication and navigation signals during SSW. We suspect that this observation of

527 ionospheric chaos may be attributed to the enhancement of the solar and lunar migrating tides

528 during SSWs, which influences the generation of electric fields through the E-region dynamo

529 mechanism (Goncharenko et al., 2021; Pedatella et al., 2014; Siddiqui et al., 2018). A study by

530 Yamazaki, (2013) compared SSW winter and non-SSW winter periods. He observed that SSW

531 events significantly amplify lunar tides, increasing the lunar tides amplitude by 3 times compared

532 to non-SSW winters. This modulation by SSW events explains the enhanced lunar tidal effects

533 during northern winter.

534 The latitudinal distribution of entropy showed a transition from chaotic to orderliness behavior in

535 the African sector during the peak, descending, and after-SSW phases, highlighting the impact of

536 SSW on the regional ionosphere of Africa sector, which leads to suppresses of orderliness behavior.

537   This observed orderliness behavior in the Africa sector's ionosphere cannot be attributed to the

538   Equatorial Electrojet (EEJ), because EEJ is typically confined to the magnetic equation ($\pm 3^0$).

539   The result of our analysis reveals that the observed orderliness behavior extends beyond the

540   equatorial boundary. We suspect that the observed suppression and consistency in orderliness

541   behavior reflects that there is modification in Equatorial Ionization Anomaly (EIA) structure of

542   Africa sector due to the forcing effect from SSW. The extension of orderliness behavior, associated

543   with low entropy values, spans from Addis Ababa (AAB) to Fayum (FYM) and Maputo (MPT),

544   indicating a significant alter in EIA structure driven by SSW influences. In our forthcoming

545   research, we will focus extensively on this orderliness behavior within the ionospheric current

546   system, particularly in the Africa equatorial region.

547   **5.0 Conclusion**

548   This study has unveiled the contributing influence of SSW on the regional ionosphere across

549   Europe and Africa by examining ionospheric chaos in the solar quiet current during the SSW

550   events of 2009 and 2021. These SSW events occurred during the solar minimum years of solar

551   cycle 24. The SSW was categorized according to the rising stratospheric temperature into six

552   phases namely precondition, ascending, peak, descending, after, and no-SSW phases. The study

553   covers 13 magnetometer stations across the Europe and Africa sector located within the

554   geographical longitude of 26° to 40° East. Magnetometer data obtained during the periods of SSW

555   were used to derive time series of the solar quiet current, Sq(H). These solar quiet current time

556   series were transformed into a network representation through the Horizontal Visibility Graph

557   (HVG) approach and analyzed by Fuzzy Entropy to quantify the presence of ionospheric chaos

558   during the periods of SSW. We found that the latitudinal distribution of entropy depicts high

559   entropy indicating the presence of ionospheric chaos in most of the stations situated within the

560 Europe sector compared to stations in the Africa sector. A consistent low entropy distribution

561 unveiling the presence of orderliness behavior were found to be prominent in the Africa sector.

562 This prevailing evidence of orderliness behavior in the Africa sector during SSW signifies that the

563 contribution influence of SSW to the regional ionosphere of Africa sector manifest an orderliness

564 behavior in its underlying dynamics. While, the pronounced features of ionospheric chaos

565 associated with high entropy values found in the Europe sector. This ionospheric chaos unveils the

566 evidence of significant effects of SSW on the regional ionosphere in Europe. Finally, we found

567 that after the peak phase of SSW, the ionospheric chaos is more pronounced.

568 **Code availability**

569 The code is a collection of routines in MATLAB (MathWorks) and is available upon request to the

570 corresponding author.

571 **Data availability**

572 The magnetometer data are publicly available and provided by Magnetic Data Acquisition System

573 (MAGDAS) at the International Research Centre for Space and Planetary Environment Science,

574 Fukuoka, Japan (http://magdas2.serc.kyushu-u.ac.jp/). The magnetometer can also be access at

575 the International Real-time Magnetic Observatory Network (INTERMAGNET) (available online

576 at www.intermagnet.org). While the stratospheric temperature can be access from National

577 Oceanic and Atmospheric Administration (NOAA) (https://psl.noaa.gov/data/getpage/). The

578 planetary index are provided and access GFZ Indices of Global Geomagnetic Activity

579 (https://www.gfz-potsdam.de/Kp-index/). The data of disturbance storm time in minute resolution

580 (SYM-H) is available at the World Data Centre for Geomagnetism, Kyoto, Japan:

581 https://wdc.kugi.kyoto-u.ac.jp/, while the solar flux index are archived at the National Aeronautics

582 and Space Administration (NASA), Space Physics Facility: https://omniweb.gsfc.

583 nasa.gov/form/dx1.html

Author contributions

584

585 **IAO** developed the idea behind the problem being solved, supervise the project, analyzed the data;

586 developed the codes; and draft the manuscript; **VA** supervise the project, developed the codes,

587 analyzed the data and contribute to the drafting of the manuscript; **MN** supervise the project and

588 contribute to the drafting of the manuscript; **OOI, BOS, and OBO** contributes to the interpretation

589 and Discussion of results; **NAN and OOT** read and made useful comments to the manuscript.

Competing interests

590

591 Some authors are members of the editorial board of nonlinear processes in geophysics journal, and

592 the authors declare they have no conflict of interest.

Acknowledgement

593

594 The authors would like to appreciate the Magnetic Data Acquisition System (MAGDAS) for

595 providing the magnetometer data used for this research upon the request from the project leader of

596 MAGDAS/CPMIN observations Dr. A. Yosikawa. We also extend our gratitude to the

597 INTERMAGNET Networks for making available the magnetometer data across the globe.

References

598

599 Azami, H., Li, P., Arnold, S. E., Escudero, J., and Humeau-Heurtier, A.: Fuzzy entropy metrics

600 for the analysis of biomedical signals: Assessment and comparison, IEEE Access, 7, 104833–

601 104847, https://doi.org/10.1109/ACCESS.2019.2930625, 2019.

602 Baldwin, M. P., Ayarzagüena, B., Birner, T., Butchart, N., Butler, A. H., Charlton-Perez, A. J.,

603 Domeisen, D. I. V., Garfinkel, C. I., Garny, H., Gerber, E. P., Hegglin, M. I., Langematz, U., and

604 Pedatella, N. M.: Sudden Stratospheric Warmings, Rev. Geophys., 59, 1–37,

605 https://doi.org/10.1029/2020RG000708, 2021.

606 Barton, C. E. and Tarlowski, C. Z.: Geomagnetic, geocentric, and geodetic coordinate

607 transformations, Comput. Geosci., 17, 669–678, https://doi.org/https://doi.org/10.1016/0098-

608 3004(91)90038-F, 1991.

609 Bolaji, O. S., Oyeyemi, E. O., Owolabi, O. P., Yamazaki, Y., Rabiu, A. B., Okoh, D., Fujimoto,

610 A., Amory-Mazaudier, C., Seemala, G. K., Yoshikawa, A., and Onanuga, O. K.: Solar quiet current

611 response in the African sector due to a 2009 sudden stratospheric warming event, J. Geophys. Res.

612 Sp. Phys., 121, 8055–8065, https://doi.org/10.1002/2016JA022857, 2016a.

613 Bolaji, O. S., Oyeyemi, E. O., Owolabi, O. P., Yamazaki, Y., Rabiu, A. B., Okoh, D., Fujimoto,

614 A., Amory-Mazaudier, C., Seemala, G. K., Yoshikawa, A., and Onanuga, O. K.: Solar quiet current

615 response in the African sector due to a 2009 sudden stratospheric warming event, J. Geophys. Res.

616 Sp. Phys., 121, 8055–8065, https://doi.org/https://doi.org/10.1002/2016JA022857, 2016b.

617 Butler, A. H., Seidel, D. J., Hardiman, S. C., Butchart, N., Birner, T., and Match, A.: Defining

618 sudden stratospheric warmings, Bull. Am. Meteorol. Soc., 96, 1913–1928,

619 https://doi.org/10.1175/BAMS-D-13-00173.1, 2015.

620 Chau, J. L., Goncharenko, L. P., Fejer, B. G., and Liu, H. L.: Equatorial and low latitude

621 ionospheric effects during sudden stratospheric warming events : Ionospheric effects during SSW

622 events, Space Sci. Rev., 168, 385–417, https://doi.org/10.1007/s11214-011-9797-5, 2012.

623 Chen, W., Wang, Z., Xie, H., and Yu, W.: Characterization of Surface EMG Signal Based on

624 Fuzzy Entropy, IEEE Trans. Neural Syst. Rehabil. Eng., 15, 266–272,

625   https://doi.org/10.1109/TNSRE.2007.897025, 2007.

626   Conejero, J. A., Velichko, A., Garibo-i-Orts, Ò., Izotov, Y., and Pham, V. T.: Exploring the

627   Entropy-Based Classification of Time Series Using Visibility Graphs from Chaotic Maps,

628   Mathematics, 12, https://doi.org/10.3390/math12070938, 2024.

629   Dass, B., Tomar, V. P., and Kumar, K.: Fuzzy entropy with order and degree for intuitionistic

630   fuzzy set, AIP Conf. Proc., 2142, https://doi.org/10.1063/1.5122619, 2019.

631   Fejer, B. G., Tracy, B. D., Olson, M. E., and Chau, J. L.: Enhanced lunar semidiurnal equatorial

632   vertical plasma drifts during sudden stratospheric warmings, Geophys. Res. Lett., 38,

633   https://doi.org/https://doi.org/10.1029/2011GL049788, 2011.

634   Gonçalves, B. A., Carpi, L., Rosso, O. A., and Ravetti, M. G.: Time series characterization via

635   horizontal visibility graph and Information Theory, Phys. A Stat. Mech. its Appl., 464, 93–102,

636   https://doi.org/10.1016/j.physa.2016.07.063, 2016.

637   Goncharenko, L. P., Chau, J. L., Liu, H.-L., and Coster, A. J.: Unexpected connections between

638   the   stratosphere   and   ionosphere,   Geophys.   Res.   Lett.,   37,

639   https://doi.org/https://doi.org/10.1029/2010GL043125, 2010.

640   Goncharenko, L. P., Coster, A. J., Plumb, R. A., and Domeisen, D. I. V: The potential role of

641   stratospheric ozone in the stratosphere-ionosphere coupling during stratospheric warmings,

642   Geophys. Res. Lett., 39, https://doi.org/https://doi.org/10.1029/2012GL051261, 2012.

643   Goncharenko, L. P., Harvey, V. L., Liu, H., and Pedatella, N. M.: Sudden Stratospheric Warming

644   Impacts on the Ionosphere-Thermosphere System: A Review of Recent Progress, 369–400 pp.,

645   https://doi.org/10.1002/9781119815617.ch16, 2021.

646 Ishikawa, A. and Mieno, H.: The fuzzy entropy concept and its application, Fuzzy Sets Syst., 2,

647 113–123, https://doi.org/10.1016/0165-0114(79)90020-4, 1979.

648 Klimenko, M. V., Bessarab, F. S., Sukhodolov, T. V., Klimenko, V. V., Koren'kov, Y. N.,

649 Zakharenkova, I. E., Chirik, N. V., Vasil'ev, P. A., Kulyamin, D. V., Shmidt, K., Funke, B., and

650 Rozanov, E. V.: Ionospheric Effects of the Sudden Stratospheric Warming in 2009: Results of

651 Simulation with the First Version of the EAGLE Model, Russ. J. Phys. Chem. B, 12, 760–770,

652 https://doi.org/10.1134/S1990793118040103, 2018.

653 Klimenko, M. V., Klimenko, V. V., Bessarab, F. S., Sukhodolov, T. V., Vasilev, P. A., Karpov, I.

654 V., Korenkov, Y. N., Zakharenkova, I. E., Funke, B., and Rozanov, E. V.: Identification of the

655 mechanisms responsible for anomalies in the tropical lower thermosphere/ionosphere caused by

656 the January 2009 sudden stratospheric warming, J. Sp. Weather Sp. Clim., 9,

657 https://doi.org/10.1051/swsc/2019037, 2019.

658 Li, C., Li, Z., Guan, L., Qi, P., Si, J., and Hao, B.: Measuring the complexity of chaotic time series

659 by fuzzy entropy, ACM Int. Conf. Proceeding Ser., Part F1305,

660 https://doi.org/10.1145/3102304.3102320, 2017.

661 Liu, H.-L., Wang, W., Richmond, A. D., and Roble, R. G.: Ionospheric variability due to planetary

662 waves and tides for solar minimum conditions, J. Geophys. Res. Sp. Phys., 115,

663 https://doi.org/https://doi.org/10.1029/2009JA015188, 2010.

664 Luque, B., Lacasa, L., Ballesteros, F., and Luque, J.: Horizontal visibility graphs: Exact results for

665 random time series, Phys. Rev. E, 80, 46103, https://doi.org/10.1103/PhysRevE.80.046103, 2009.

666 Maute, A., Hagan, M. E., Richmond, A. D., and Roble, R. G.: TIME-GCM study of the ionospheric

667 equatorial vertical drift changes during the 2006 stratospheric sudden warming, J. Geophys. Res.

Sp. Phys., 119, 1287–1305, https://doi.org/https://doi.org/10.1002/2013JA019490, 2014.

O'Pella, J.: Horizontal visibility graphs are uniquely determined by their directed degree sequence, Phys. A Stat. Mech. its Appl., 536, 120923, https://doi.org/10.1016/j.physa.2019.04.159, 2019.

Pedatella, N. M., Liu, H.-L., Sassi, F., Lei, J., Chau, J. L., and Zhang, X.: Ionosphere variability during the 2009 SSW: Influence of the lunar semidiurnal tide and mechanisms producing electron density variability, J. Geophys. Res. Sp. Phys., 119, 3828–3843, https://doi.org/https://doi.org/10.1002/2014JA019849, 2014.

Siddiqui, T. A., Maute, A., Pedatella, N., Yamazaki, Y., Lühr, H., and Stolle, C.: On the variability of the semidiurnal solar and lunar tides of the equatorial electrojet during sudden stratospheric warmings, Ann. Geophys., 36, 1545–1562, https://doi.org/10.5194/angeo-36-1545-2018, 2018.

Yamazaki, Y.: Large lunar tidal effects in the equatorial electrojet during northern winter and its relation to stratospheric sudden warming events, J. Geophys. Res. Sp. Phys., 118, 7268–7271, https://doi.org/10.1002/2013JA019215, 2013.

Yamazaki, Y.: Solar and lunar ionospheric electrodynamic effects during stratospheric sudden warmings, J. Atmos. Solar-Terrestrial Phys., 119, 138–146, https://doi.org/10.1016/j.jastp.2014.08.001, 2014.

Yamazaki, Y. and Maute, A.: Sq and EEJ—A Review on the Daily Variation of the Geomagnetic Field Caused by Ionospheric Dynamo Currents, Space Sci. Rev., 206, 299–405, https://doi.org/10.1007/s11214-016-0282-z, 2017.

Yamazaki, Y. and Richmond, A. D.: A theory of ionospheric response to upward-propagating tides: Electrodynamic effects and tidal mixing effects, J. Geophys. Res. Sp. Phys., 118, 5891–

689   5905, https://doi.org/https://doi.org/10.1002/jgra.50487, 2013.

690   Yamazaki, Y., Yumoto, K., Uozumi, T., and Cardinal, M. G.: Intensity variations of the equivalent

691   S current system along the 210° magnetic meridian, J. Geophys. Res. Sp. Phys., 116,

692   https://doi.org/https://doi.org/10.1029/2011JA016632, 2011.

693   Yamazaki, Y., Yumoto, K., McNamara, D., Hirooka, T., Uozumi, T., Kitamura, K., Abe, S., and

694   Ikeda, A.: Ionospheric current system during sudden stratospheric warming events, J. Geophys.

695   Res. Sp. Phys., 117, 1–7, https://doi.org/10.1029/2011JA017453, 2012a.

696   Yamazaki, Y., Richmond, A. D., Liu, H., Yumoto, K., and Tanaka, Y.: Sq current system during

697   stratospheric sudden warming events in 2006 and 2009, J. Geophys. Res. Sp. Phys., 117,

698   https://doi.org/https://doi.org/10.1029/2012JA018116, 2012b.

699   Zou, Y., Donner, R. V., Marwan, N., Donges, J. F., and Kurths, J.: Complex network approaches

700   to   nonlinear   time   series   analysis,   Phys.   Rep.,   787,   1–97,

701   https://doi.org/10.1016/j.physrep.2018.10.005, 2019.

702

703

704
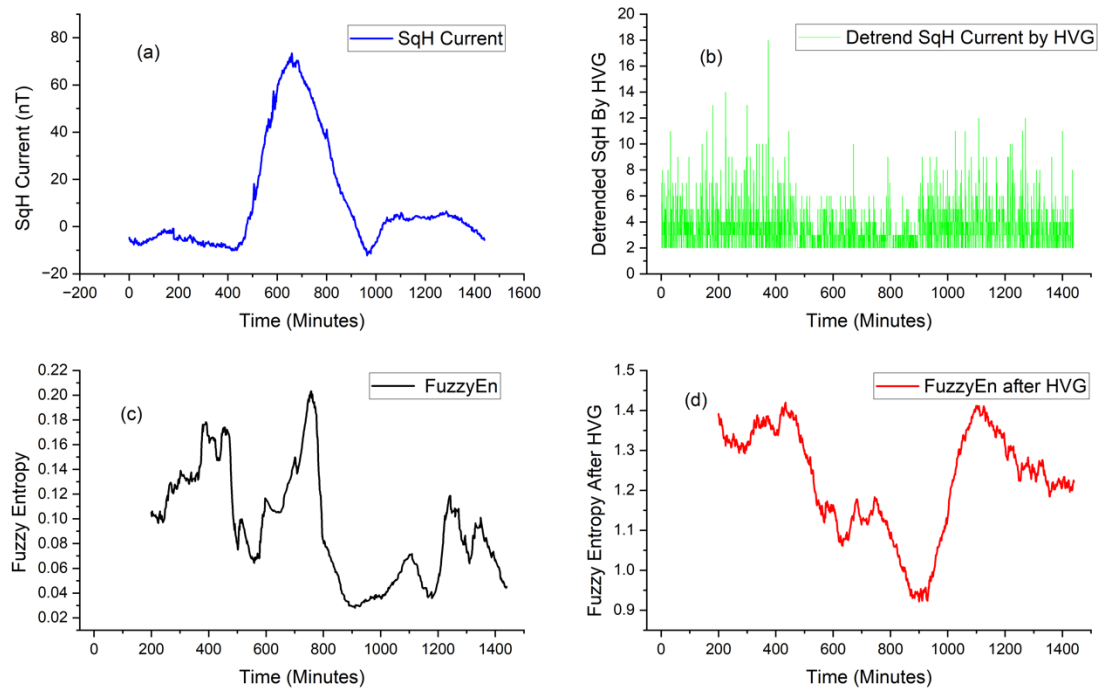
Figure 6: The sample of solar quiet current Sq(H) on 31st of March 2009 at Addis Ababa, Ethiopa:
(a) The time series of solar quiet current, Sq(H) derived in minutes, (b) The detrended time series
of solar quiet current transformed through Horizontal Visibility Graph (HVG), (c) The changes in
Fuzzy Entropy of solar quiet current without HVG transformation, (d) The changes in Fuzzy
Entropy of solar quiet current with HVG transformation.

710

711

712
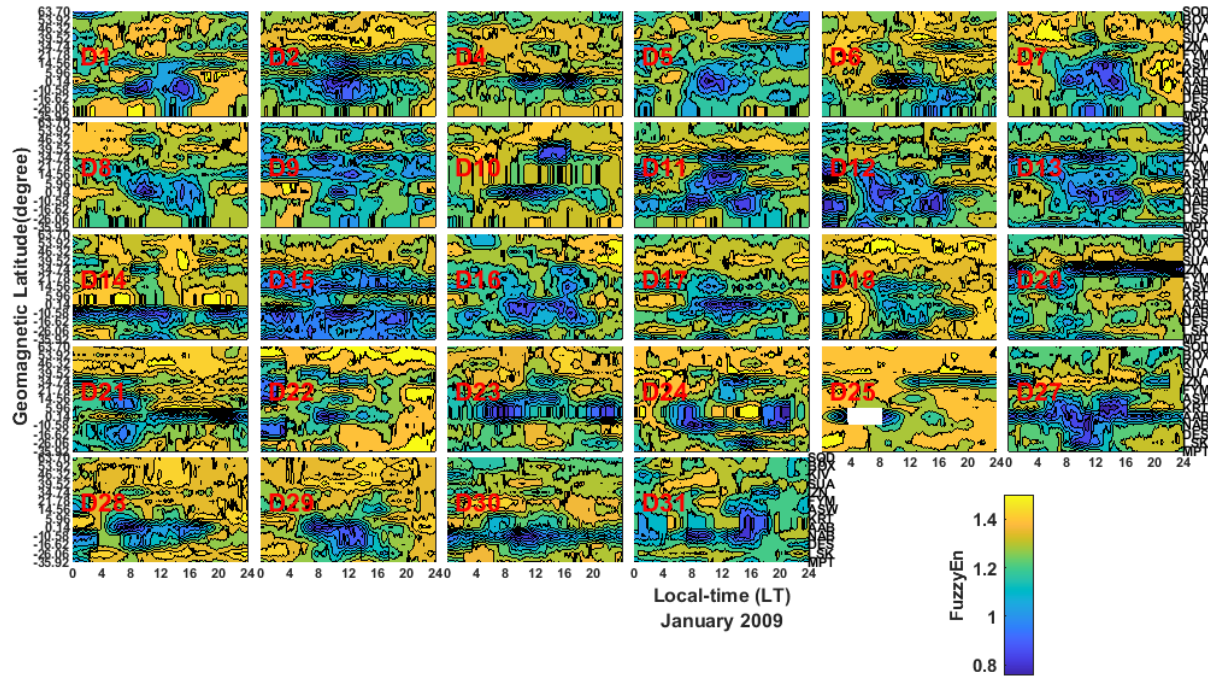
Figure 7: The Day-to-Day latitudinal Distribution of Fuzzy Entropy across Europe-Africa sector

on January 2009

715
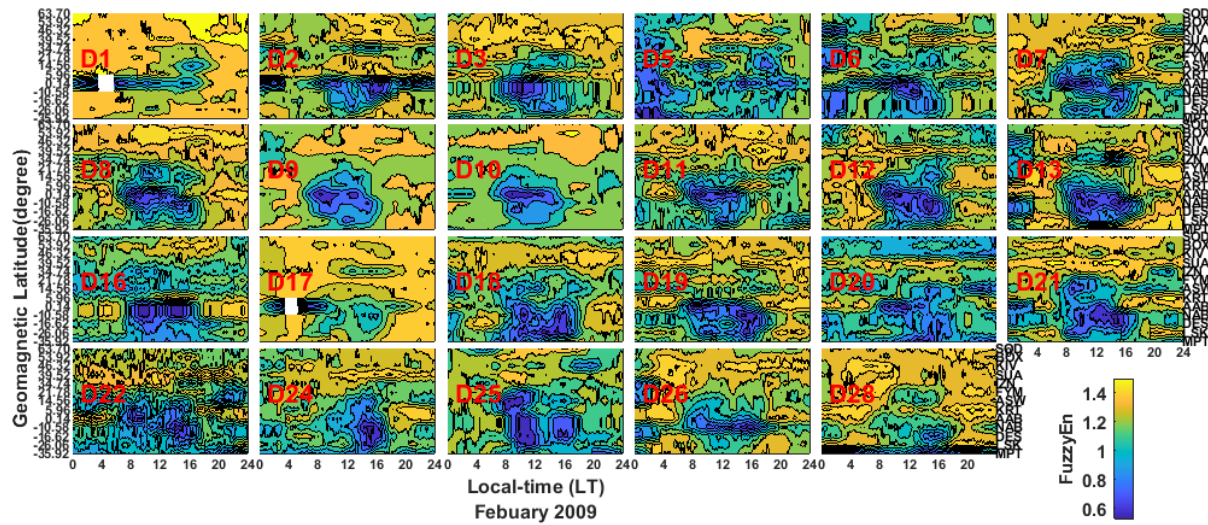
Figure 8: The Day-to-Day latitudinal Distribution of Fuzzy Entropy across Europe-Africa sector

on February 2009.

718
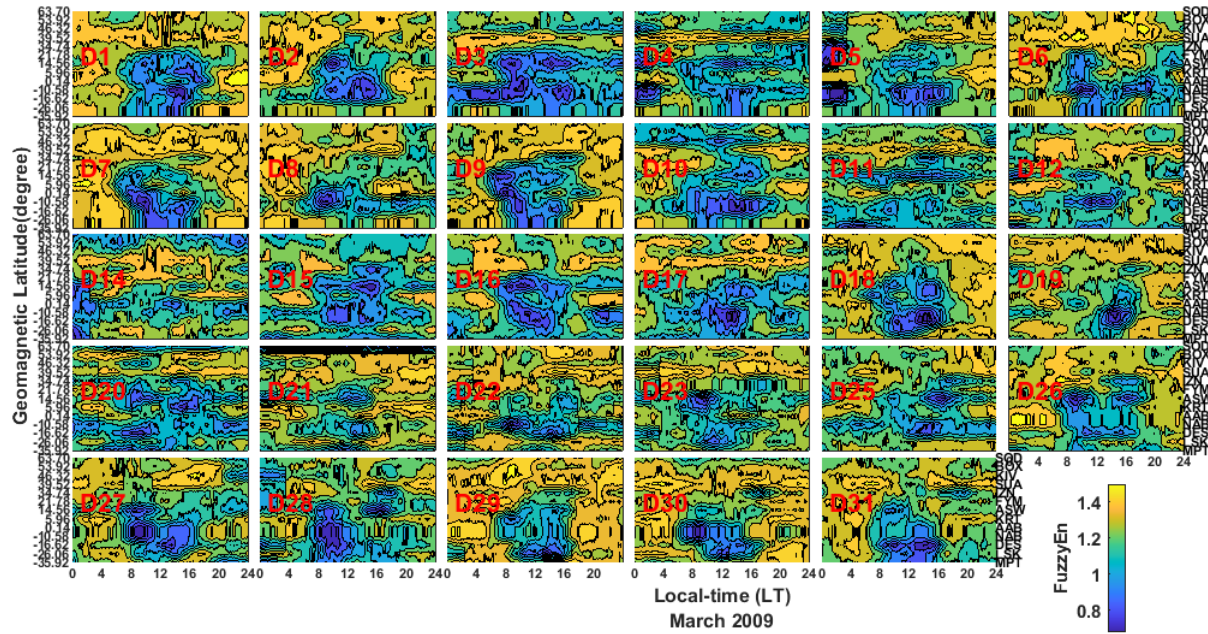
Figure 9: The Day-to-Day latitudinal Distribution of Fuzzy Entropy across Europe-Africa sector

on March 2009

721
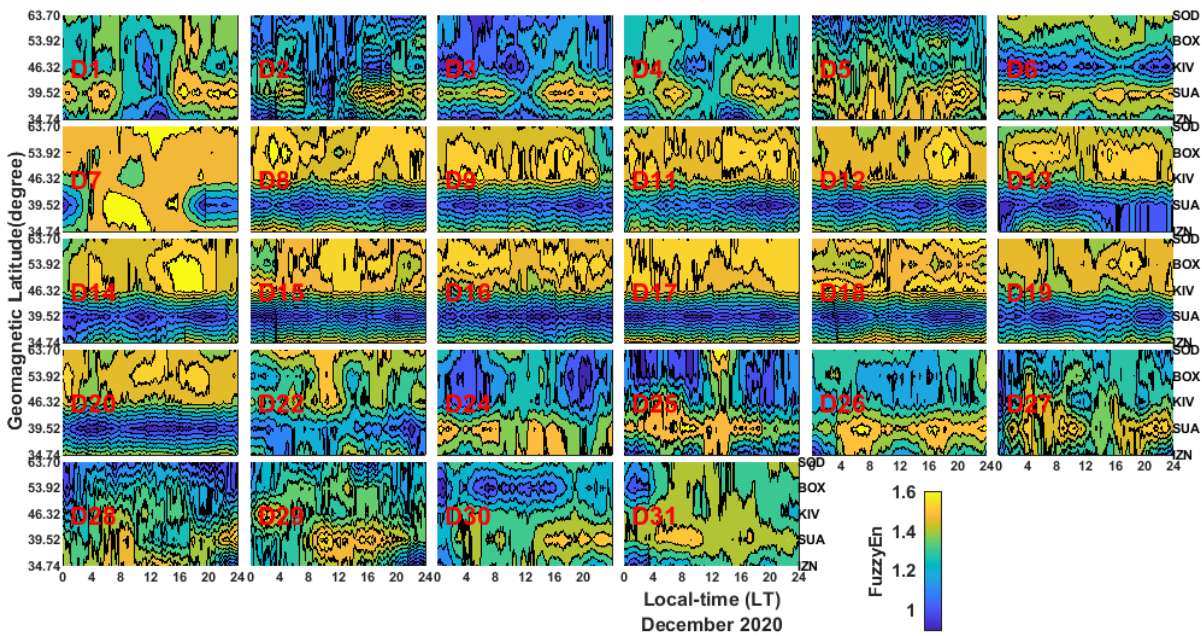
Figure 10: The Day-to-Day latitudinal Distribution of Fuzzy Entropy across Europe sector on

December 2020

724
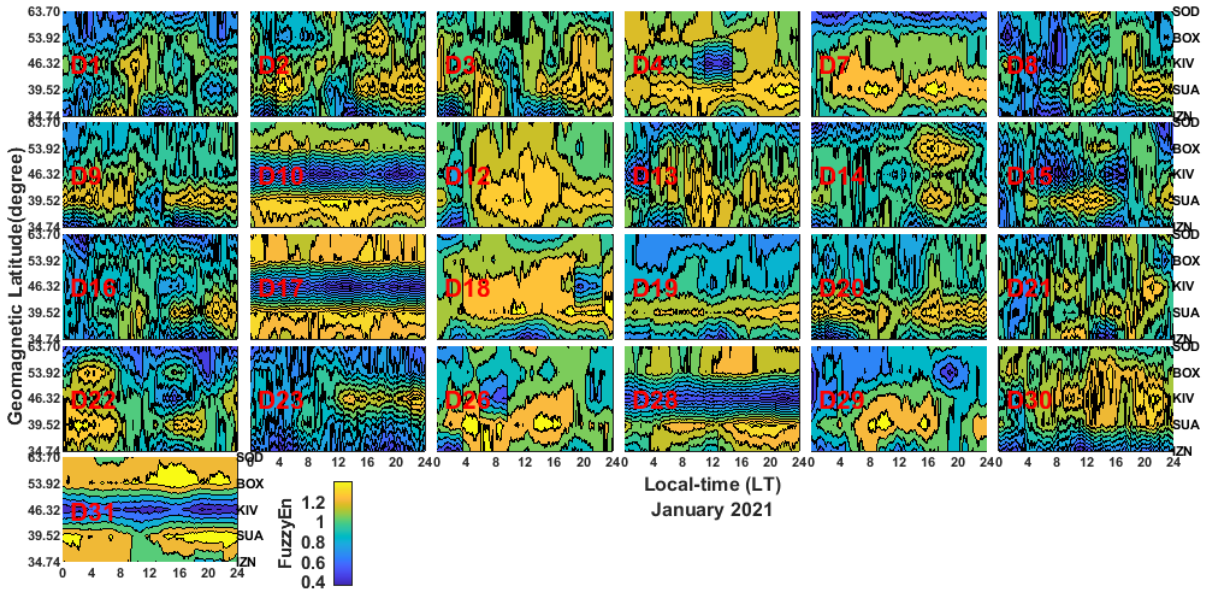
Figure 11: The Day-to-Day latitudinal Distribution of Fuzzy Entropy across Europe sector on

January 2021.

727
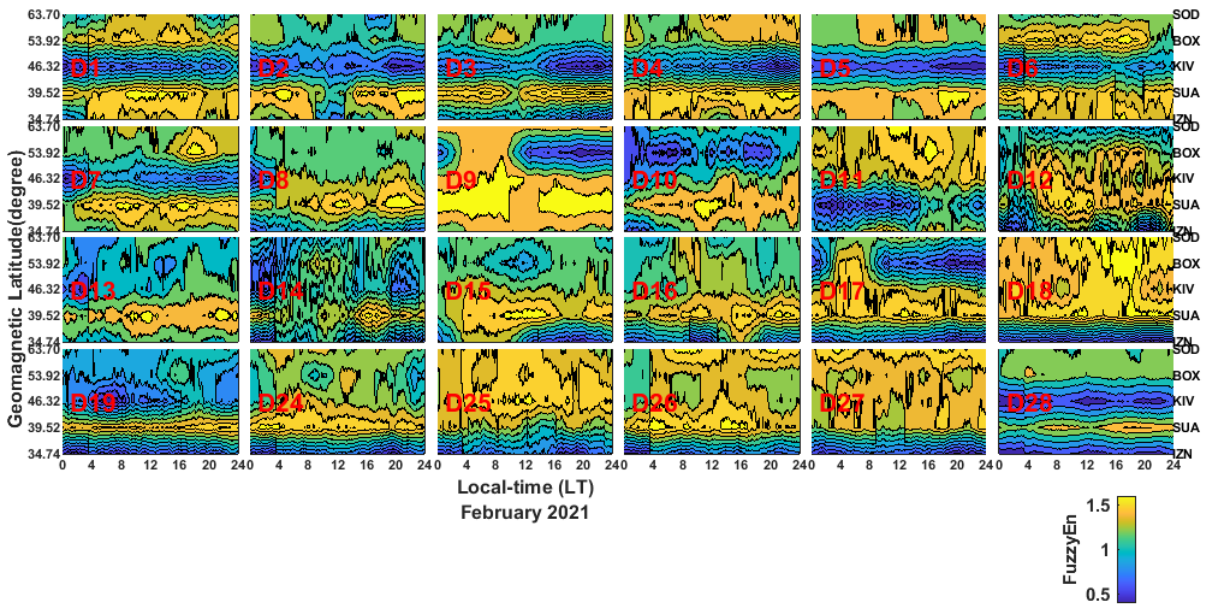
Figure 12: The Day-to-Day latitudinal Distribution of Fuzzy Entropy across Europe sector on

February 2021.
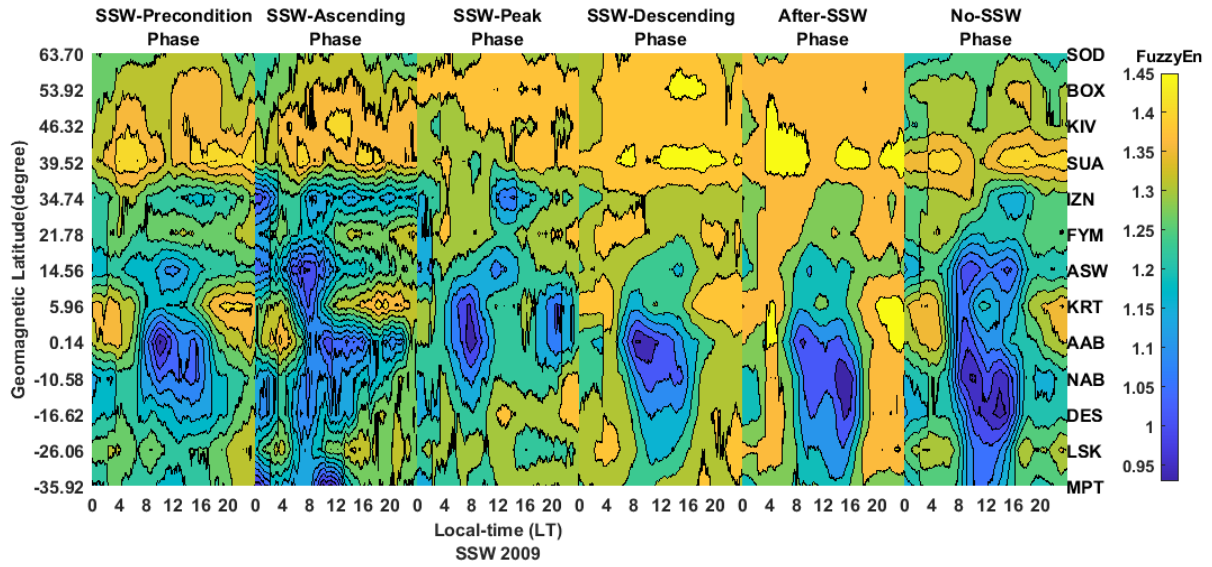
Figure 13: The latitudinal distribution of Fuzzy Entropy across Europe-Africa sector during the

phases of 2009 SSW.
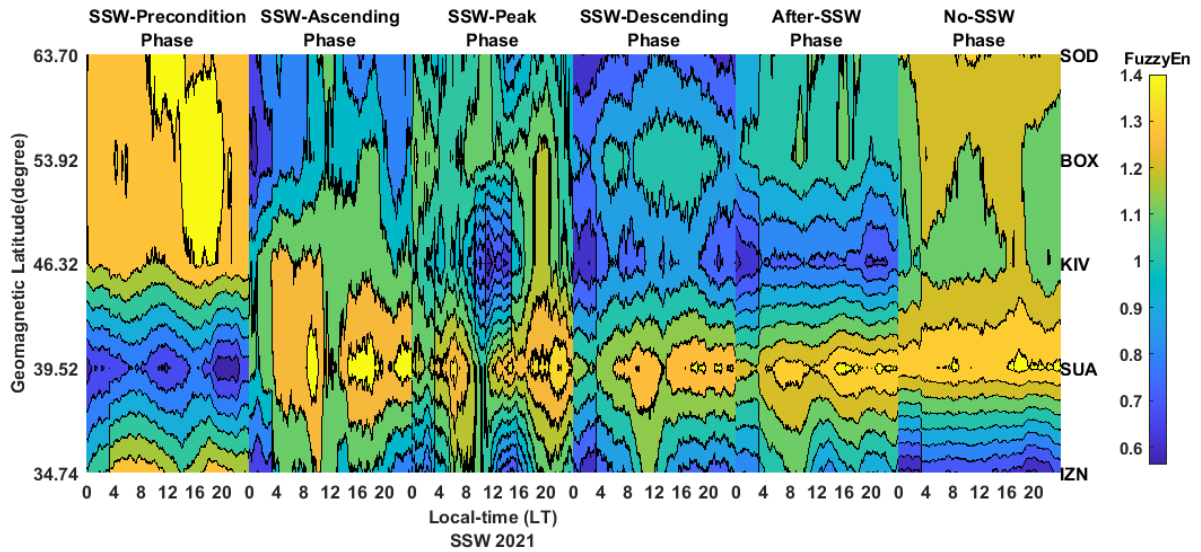
Figure 14: The latitudinal distribution of Fuzzy Entropy across Europe sector during the phases

of 2021 SSW.